



City Research Online

City, University of London Institutional Repository

Citation: Xu, G., Zhou, Y., Yan, S. & Zhang, N. (2022). Numerical investigation of wave amplitude spectra effects on focusing wave generation. *Ocean Engineering*, 265, 112550. doi: 10.1016/j.oceaneng.2022.112550

This is the published version of the paper.

This version of the publication may differ from the final published version.

Permanent repository link: <https://openaccess.city.ac.uk/id/eprint/29125/>

Link to published version: <https://doi.org/10.1016/j.oceaneng.2022.112550>

Copyright: City Research Online aims to make research outputs of City, University of London available to a wider audience. Copyright and Moral Rights remain with the author(s) and/or copyright holders. URLs from City Research Online may be freely distributed and linked to.

Reuse: Copies of full items can be used for personal research or study, educational, or not-for-profit purposes without prior permission or charge. Provided that the authors, title and full bibliographic details are credited, a hyperlink and/or URL is given for the original metadata page and the content is not changed in any way.

City Research Online:

<http://openaccess.city.ac.uk/>

publications@city.ac.uk



Numerical investigation of wave amplitude spectra effects on focusing wave generation

Guochun Xu^a, Yan Zhou^{b,*}, Shiqiang Yan^c, Ningbo Zhang^{c,d}

^a Faculty of Maritime and Transportation, Ningbo University, Ningbo, Zhejiang, China

^b School of Engineering, University of Liverpool, Liverpool, UK

^c School of Engineering and Mathematical Sciences, City University of London, London, UK

^d College of Shipbuilding Engineering, Harbin Engineering University, Harbin, Heilongjiang, China

ARTICLE INFO

Keywords:

Focusing wave generation
Wave amplitude spectra
Focusing wave crest elevation
Focusing position

ABSTRACT

Focusing waves are often considered as an effective simulation of freak waves observed in oceans, or extreme sea states for marine structures design. The understanding of factors in generating prescribed focusing wave is of great importance for its generation in both numerical and physical wave tank. Based on the fully nonlinear potential theory solved by the QALE-FEM, this paper numerically investigates the effect of wave amplitude distribution over the frequency band under a series of the crest elevation parameters and frequency ranges on focusing wave generation, including focusing wave crest elevations and focusing positions. The results suggest that focusing wave crest elevation is significantly affected by the wave amplitude distribution especially for target waves with large wave crests or those are assigned at low frequency domain. Moreover, generation positions of focusing wave are also strongly correlated to amplitude spectra through phase shift of the wave surface and wave nonlinearity denoted by wave steepness.

1. Introduction

Freak waves (also called rogue waves) are extreme water waves in the ocean, which can bring severe hazards to mariners, coastal and offshore structures, and navigational vessels. As reported during 2011–2018 (Didenkulova, 2020), freak waves killed 386 people and made 24 ships sunk. To investigate how freak waves impact on ocean structures, it is of great importance to reproduce extreme wave events in either physical or numerical wave tanks. Wave focusing is one of the mechanisms in generation of freak waves (Kharif and Pelinovsky, 2003; Fochesato et al., 2007; Shemer and Ee, 2015), and is often adopted to simulate freak waves, such as the New Year Wave (Clauss and Klein, 2011). Thus, deep understanding of focusing wave generation, particularly the effects of the amplitude distribution of wave components, is crucial to effectively mimic freak wave events.

For focusing wave generation, several methods have been proposed based on various mechanisms. Modifying the external conditions such as topography, currents or wind can lead to wave energy focus and produce focusing waves (Zheng et al., 2020; Manolidis et al., 2019; Wu and Yao, 2004; Kharif et al., 2008). Focusing waves can be also generated by nonlinear self-focusing through adjusting characteristic parameters (e.

g., frequency bandwidth or wave number) of a wave group, either to focus wave energy on certain side-bands (Zhang et al., 2019), or to induce wave resonance among wave components (Fujimoto et al., 2019). For narrow-banded waves in deep and intermediate-depth water, the nonlinear Schrödinger (NLS) equation is usually employed to analyze the nonlinear focusing features (Shemer, 2015). If the spectral width is not imposed any constraints, the Zakharov equation proposed by (Shemer et al., 2001) can be considered as a theoretical model to qualitatively and quantitatively described the slow spatial variation of the self-focusing wave groups. Several breather-solutions of abnormal waves generated based on the self-focusing mechanism have been developed and verified (Chabchoub et al., 2012, 2014; Yuen and Lake, 1980; Onorato and Soret, 2016). Sometimes, they are chosen as typical design waves by some researchers (Klein et al., 2016, 2021) to investigate hydrodynamic impact on marine structures under extreme sea states since these breathers could be analytically solved and are up to physically possible wave elevations under certain frequency. Another mechanism used to generate focusing waves is the linear superposition principle of wave energy (also called the spatial-temporal focusing mechanism), originally introduced by (Davis and Zarnick, 1964) to generate transient waves based on a ‘sweep frequency’ technique, and

* Corresponding author.

E-mail address: yan.zhou@liverpool.ac.uk (Y. Zhou).

<https://doi.org/10.1016/j.oceaneng.2022.112550>

Received 14 January 2022; Received in revised form 25 April 2022; Accepted 11 September 2022

Available online 29 September 2022

0029-8018/© 2022 The Authors. Published by Elsevier Ltd. This is an open access article under the CC BY license (<http://creativecommons.org/licenses/by/4.0/>).

further developed by (Takezawa and Hirayama, 1976) so as to control the shape of the initial wave spectrum. Based on the principle, there summarizes as the wave dispersive method (Touboul et al., 2006) and the phase modulation method (Baldock et al., 1996). The former utilizes the variation of dispersion properties of the wave components and generates the components in descending order of the frequency. The latter is achieved by phase modulation which forces the amplitudes of wave components simultaneously arrive at their maximums at specific time and position.

Comparing above mechanisms used to generate focusing waves, modifying the external condition and nonlinear self-focusing are difficult to accurately specify wave profiles or their generating positions especially for focusing waves with higher and steeper profile. Therefore, to obtain predefined focusing waves in wave tanks, the linear superposition of wave energy is more widely used in generation scheme. Its dispersive method is barely adopted for the physical wave tank as it contains high frequency components which may go beyond the capacity of the wave maker. Meanwhile, since it is more practical to modify each wave component in wave generation, the phase modulation method is more commonly employed to generate focusing waves for studying the hydrodynamic responses of ocean structures under tailored extreme wave states (Ma et al., 2015; Gong et al., 2021; Greenhow et al., 1982; Deng et al., 2016) and is also adopted in this study.

It is widely recognized that the actually registered wave spectra and the resulting focusing waves generated in wave tank, either physically or numerically, are often different from their corresponding target ones. To successfully produce expected focusing waves, several improvements have been developed based on the phase modulation method. Considering the fact that short and high wave groups have strong nonlinearity, an additional celerity term is considered respectively based on iterative integration of coupled equations of particle tracks (Kuehnlein et al., 2002) and the Stokes third order theory (Hennig, 2005), and then the motion signal of wave board is amended to accurately generate transient focusing wave surface at specified position of wave tank. A phase iteration scheme, which modifies the phases of the wave components for them to better converge to zero at the assigned positions was proposed (Chaplin, 1996). For better determining wave component phases at each iteration, Clauss et al. (2006) introduced an optimizing scheme based on the Nelder-Mead Simplex method. On top of the phase iteration, Schmittner et al. (2009) added an iteration of wave component amplitudes in focusing wave generation. In the new phase-amplitude iteration scheme, the amplitude of each wave component is modified by the ratio of its target amplitude and the generated amplitude. However, the modification would cause the wave components deviating from the expected ones due to large error introduced in the amplitude iteration (Deng et al., 2016). To overcome the difficulty, the changing ratio of component amplitudes by their wave energy at the corresponding frequency intervals was calculated (Ma et al., 2015). Nevertheless, when the phase-amplitude iteration scheme is applied to generate focusing waves in the physical wave tank, the time history of the wave free surface cannot be recorded long enough because of reflective waves. Consequently, wave component amplitudes may not be correctly calculated by the Fast Fourier Transform (FFT) for the limited time history of wave free surface record. Niu et al. (2020) and Stagonas et al. (2018) found that the phase-amplitude iteration scheme became less effective because of incorrect amplitudes of wave components. To accurately decide the amplitudes of free wave components in each iteration, Khait and Shemer (2018) decomposed the complex amplitude spectrum of the surface elevation into free and bound components based on the spatial Zakharov equation.

Focusing waves are determined by the assigned characteristic parameters (i.e., input wave crest parameter, specified focusing position and time, frequency range, and wave component amplitude spectrum). In general, when large wave crest parameters are input, the actually generated focusing wave crest elevations can significantly exceed their initially specified ones (Yan and Ma, 2012; Ning et al., 2012; Ai et al.,

2014; Li and Liu, 2015). The focusing position and time parameter affect wave generation in a combined way, i.e., for one with fixed focusing position, only when the given focusing time is larger than a critical value, the focusing wave is likely to be accurately generated (Xu et al., 2019). As for frequency range, it may be broadened, reduced or shifted (i.e., keeping the bandwidth constant and moving the frequency range). Most of studies focus on widening or narrowing frequency ranges, and find that narrower bandwidths will generate larger focusing wave crest elevations (Baldock et al., 1996; Ai et al., 2014; Xu et al., 2019). Nevertheless, studies on the shift of frequency range are very limited (Li and Liu, 2015) presenting numerical investigations based on cases with bandwidth being 0.56Hz.

Wave amplitude spectrum containing the amplitude distribution of wave components over the assigned frequency range, is also a significant parameter for focusing wave generation. Several wave amplitude spectra, such as the Gaussian amplitude distribution employed in early days to analytically analyze evolving process of focusing waves (Clauss and Bergmann, 1986), the constant wave amplitude spectrum (CWA) (Baldock et al., 1996) and the constant wave steepness spectrum (CWS) (Hennig, 2005), have been investigated. Chaplin (1996) found that the breaking criteria of focusing waves was affected by wave component amplitude distribution. The influence of the amplitude spectrum for nonbreaking waves was also confirmed in comparison of focusing waves based on the CWA, the CWS and the amplitude distribution given by JONSWAP spectrum (Li and Liu, 2015). More comparisons are conducted between focusing waves produced by the CWS and a linear slope steepness spectrum (Wu and Yao, 2004). Additionally, for focusing waves based on the quasi-CWA (QCWA) spectrum and the quasi-CWS (QCWS), experimental investigations conducted by Xu et al. (2019) indicate that the amplitudes of high-frequency components play an important role on the shape and crest elevation of focusing waves. According to the existing focusing wave generation research base on the linear superposition principle of wave energy for both in the physical tank and by numerical simulation, the influence of wave amplitude spectrum on focusing wave generation has been widely identified. While to the best knowledge of the authors, systemic analysis of how the wave amplitude distribution in wave spectrum affects the focusing crest elevation and position has not been performed.

In this study, to explore the effects of the amplitude distribution in wave spectrum on the wave crest elevation and generating position, and therefore to effectively guide wave spectrum selection and construction for focusing wave generation, three amplitude spectra, will be designed containing the same wave energy but different amplitude distributions. Focusing wave crest elevations and positions corresponding to each type of distribution under a range of wave crest parameters and central frequencies will be analyzed to deeply understand the influences of wave amplitude spectra distribution on them. Investigations are performed in a numerical wave tank, which is established based on the fully nonlinear potential theory (FNPT), solved by the quasi arbitrary Lagrangian-Eulerian finite element method (QALE-FEM) and the Modified Simplified Finite Difference Interpolation method (MSFDI).

2. Mathematical model and numerical methods

In this paper, a 2D rectangular numerical wave tank is set up as shown in Fig. 1. A flap-type wave maker is arranged at the left side, and a damping zone with the Sommerfeld condition is imposed at the right side of the tank to suppress the wave reflection. The Cartesian coordinate system is adopted, and its origin is at the mean free surface. The x-axis is along the length of the tank, and the z-axis is positive upwards. A series of numerical wave gauges are used for recording wave surfaces in the numerical wave tank.

2.1. Fully nonlinear potential theory (FNPT)

Following the FNPT (Ma and Yan, 2006), the fluid is assumed to be

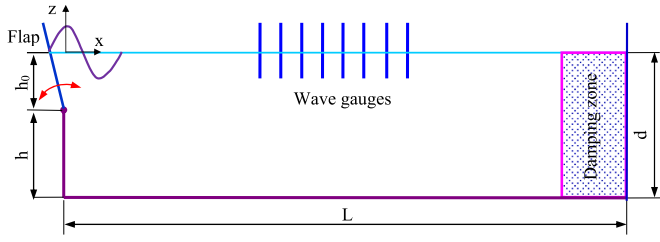


Fig. 1. Numerical wave tank consisting of flap wave generator, wave absorber and wave surface gauges.

incompressible, inviscid and irrotational, and surface tension is neglected. With the velocity potential function ϕ , the fluid velocity can be expressed by $\mathbf{u} = \nabla\phi$, and the velocity potential ϕ satisfies the Laplace equation as

$$\nabla^2\phi = 0 \quad (1)$$

On the free surface, $z = \eta(x, y, z, t)$, the kinematic and dynamic conditions are written by the Lagrangian form as Eqs. (2) and (3), respectively.

$$\frac{Dx}{Dt} = \frac{\partial\phi}{\partial x}, \frac{Dy}{Dt} = \frac{\partial\phi}{\partial y}, \frac{Dz}{Dt} = \frac{\partial\phi}{\partial z} \quad (2)$$

$$\frac{D\phi}{Dt} = -gz + \frac{1}{2}|\nabla\phi|^2 \quad (3)$$

in which $\frac{D}{Dt}$ denotes the total time derivative, and \mathbf{g} is gravitational acceleration. The pressure on wave free surface is zero.

On all rigid surfaces, including the wave flap, the side walls and the tank bed, the boundary condition is expressed by

$$\frac{\partial\phi}{\partial\mathbf{n}} = \mathbf{n} \cdot \mathbf{U}(t) \quad (4)$$

where $\mathbf{U}(t)$ is the velocity of the rigid boundary and \mathbf{n} is the unit normal vector pointing out the fluid domain. For static rigid boundaries, their velocities are zero, which simplifies the Eq. (4) as

$$\frac{\partial\phi}{\partial\mathbf{n}} = 0 \quad (5)$$

In addition to above boundary conditions, at the far end of the numerical tank, the damping zone is governed by the Eq. (6) by applying the Sommerfeld condition.

$$\frac{\partial\phi}{\partial t} + \mathbf{c} \frac{\partial\phi}{\partial\mathbf{n}} = 0 \quad (6)$$

\mathbf{n} in Eq. (6) is the outward unit normal vector of the truncated boundary and \mathbf{c} is the phase velocity of the characteristic wave. In the damping zone, an artificial viscous term is imposed to the dynamic condition of the free surface as Eq. (7).

$$\frac{D\phi}{Dt} = -gz + \frac{1}{2}|\nabla\phi|^2 - \nu(x)|\phi|\text{sign}\left(\frac{\partial\phi}{\partial\mathbf{n}}\right) \quad (7)$$

in which $\nu(x)$ is the damping coefficient, and $\text{sign}()$ is a notation function.

2.2. Numerical methods

The potential function ϕ described by the Eqs. (1)–(7) is solved by the QALE-FEM, which is developed by Ma and Yan (2006). With various key numerical techniques developed, including the interior nodes movement, the free surface nodes redistribution, the advanced velocity schemes, the QALE-FEM is validated to be accurate and efficient for fully nonlinear water wave problems and complex interactions between

strongly nonlinear waves and structures. In this research, the QALE-FEM will be adopted for simulating focusing waves.

To implement the QALE-FEM, one time step marching is carried out. The position of the free surface and the velocity potential values on it are either initially assigned or obtained by integrating Eqs. (2) and (3) at previous time step. The boundary condition on the free surface can be expressed by the Dirichlet condition, as

$$\phi = \phi_f \quad (8)$$

The potential function at each time step can be obtained by solving a mixed boundary value problem (MBVP), which is defined by Eqs. (1), (4) and (6)–(8). The key procedure for focusing wave simulation in this study is summarized in Fig. 2 and more details of the QALE-FEM can be found in references (Ma and Yan, 2006, 2009; Yan and Ma, 2010).

Since the gradient of the potential function plays a significant role in determining the position of free surface and the value of ϕ for at each time step, in this work we adopted a new gradient method MSFDI based on Ma (2008) which has been validated better accuracy and higher efficiency (Xu et al., 2015).

3. Focusing wave generation in numerical wave tank

Focusing waves are generated based on the spatio-temporal focusing mechanism by setting the focusing position x_f and time t_f . The wave free surface is expressed as

$$\eta(x, y, t) = \sum_{n=1}^N a_n \cos[k_n(x - x_f) - 2\pi f_n(t - t_f)] \quad (9)$$

where N is the total number of wave components; k_n and f_n are wave number and frequency of the n th wave component respectively with the relationship of $(2\pi f_n)^2 = gk_n \tanh(k_n d)$. Within the frequency range of $[f_1, f_N]$, f_n is linearly varied as

$$f_n = f_1 + (n - 1) \times \frac{f_N - f_1}{N - 1} \quad (10)$$

a_n is the wave amplitude of the n th component, which is given by the wave amplitude distribution. For investigating the effect of wave amplitude distributions on focusing wave generation, three distribution forms containing the same energy are created as shown in Fig. 3.

The first amplitude distribution is the Large Wave Amplitude at Low frequency (LWAL) converted based on the QCWS spectrum proposed by Xu et al. (2019). As the water depth approaches infinite in the QCWS spectrum, it transfers to the LWAL spectrum with each wave amplitude calculated by

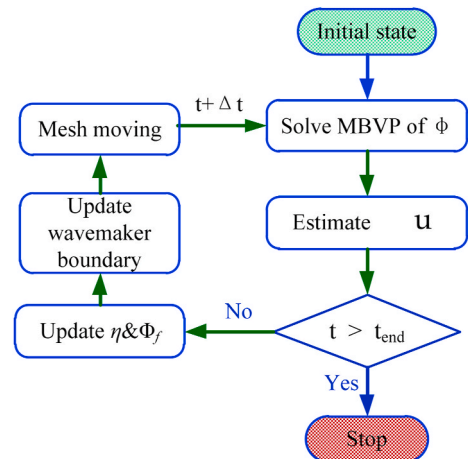


Fig. 2. Flow chart for simulating focusing waves in QALE-FEM.

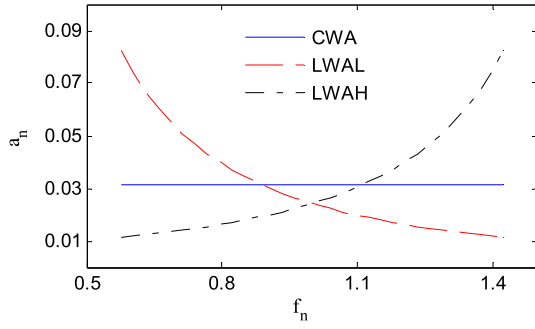


Fig. 3. Three amplitude distributions of wave components for focusing wave generation.

$$a_n = \frac{A_f}{k_n \sum_{n=1}^N 1/k_n} \quad (11)$$

where, A_f is the target focusing wave crest elevation. The expression of LWAL spectrum in Eq (11) is identical with the definition of the CWS spectrum as given in Introduction. For highlighting the topic of this paper which to investigate wave amplitude distributions, the spectrum expressed by Eq (11) is named as LWAL spectrum here after. As illustrated by the red broken line in Fig. 3, the LWAL provides high amplitudes at lower frequency and a gradual decrease of the amplitudes with frequency increases.

The second distribution form is the Constant Wave component Amplitude (CWA) with the amplitudes of each component evenly distributed across the frequency range and expressed as,

$$a_n = \frac{A_f}{N} \quad (12)$$

The third is the Large Wave Amplitude at High frequency (LWAH) spectrum for which the amplitudes continuously increase with the increase of their frequencies as expressed in Eq. (13)

$$a_n = \frac{A_f}{k_{N-n+1} \sum_{n=1}^N 1/k_n} \quad (13)$$

The amplitude in the LWAH distribution presents an opposite trend to the LWAL spectrum over the wave frequency range with higher amplitudes located at the higher frequencies.

Once the focusing wave parameters, i.e., A_f , f_n , a_n , x_f and t_f are specified, the focusing wave surface at the wave maker can be obtained by Eq. (9). According to the linear wave generation theory, the rotating angular $\theta(t)$ of the wave flap is calculated by

$$\theta(t) = \sum_{n=1}^N \frac{a_n}{F_n} \cos[2\pi f_n t + (k_n x_f - 2\pi f_n t_f)] \quad (14)$$

where F_n is the transfer function (Biesel and Suquet, 1951) between the generated wave free surface elevation and the corresponding rotating angle of the flap which can be expressed as

$$F_n = \frac{4(2\pi f_n)^2 \cosh(k_n d) [\cosh(k_n(d-h_0)) - \cosh(k_n d) + k_n d \sin(k_n d)]}{g k_n^2 (2k_n d + \sinh(2k_n d))} \quad (15)$$

in which h_0 is the length of the wave paddle below the mean free surface. According to linear wave generation theory, a phase shift of $-\pi/2$ exists between the far-field wave surface expressed by Eq (9) and the corresponding rotating angle $\theta(t)$ in Eq (14). For generating focusing wave with the wave group superposed, this phase shift phenomenon does affect the far field wave which will be discussed in the section 5.3 but not exactly following this $-\pi/2$ relationship. In addition, wave

amplitude distribution also affects phase shift of the wave surfaces and may further result in differences of focusing positions. Therefore, the rotating angle $\theta(t)$ is not modified, neither for the surface expression as in Eq. (9). By defining the angular velocity Ω as $d\theta/dt$, the velocity at a point on wave flap surface is determined by

$$\mathbf{U}_f = \Omega \times \mathbf{r}_b \quad (16)$$

where Ω is written as $[0 \ \Omega_y \ 0]$ and \mathbf{r}_b is the vector from the rotational hinge to the point on the wave flap.

The angular motion calculated by Eq (14) cannot be directly employed to generate focusing waves because of nonzero displacement appearing at initial instant. If the theoretical signal is directly employed to generate waves in numerical wave tank, the generated wave surface may have sawtooth problem, or the numerical simulation may break due to bad convergence. In this study, an inserting and extending scheme proposed by (Xu et al., 2019) is employed to generate the practicable motion signal of wave flap.

4. Numerical convergence and validation

The numerical tank for focusing wave simulation has the length of $L = 200\text{m}$ and the depth of $d = 3.5\text{m}$. The depth h from the rotating hinge of the flap to the tank bottom is 1.64m . The dimension of this numerical wave tank is similar to that of the towing tank for the physical experiments (Xu et al., 2019), except that the length of the numerical tank is longer by adding the numerical damping zone. According to the tests on damping zone in Ma et al. (2001), its length L_m is taken as the smaller value of $3\lambda_s$ and $3d$, where λ_s is the characteristic wave length defined as the minimum wave length of wave components.

4.1. Convergence tests

The convergence tests regarding mesh size and time step are carried out for the wave with $A_f = 0.1\text{m}$, $x_f = 30\text{m}$, $f_n = 0.1695\text{--}0.4545\text{Hz}$, $t_f = 36\text{s}$, and $N = 32$. By fixing ds to be $\lambda_s/35$, Δt is set to be $T_m/70$, $T_m/100$ and $T_m/200$, where T_m is the minimum period of the wave components. The time histories of wave surfaces with different time step lengths are demonstrated in Fig. 4 (a). The discrepancy between the free surfaces obtained from $\Delta t = T_m/100$ and $\Delta t = T_m/200$ is negligible, which suggests that the numerical result has converged when the time step is smaller than $T_m/100$. Thus, the time step is taken as $T_m/200$ in following simulations.

For the tests on the mesh size, the time step length is fixed as $T_m/200$, while ds is set to be $\lambda_s/10$, $\lambda_s/20$, $\lambda_s/35$ and $\lambda_s/45$. As shown in Fig. 4 (b), difference of free surfaces at the wave crest is negligible when the mesh size is smaller than $\lambda_s/20$. Mesh size will be $\lambda_s/35$ in following

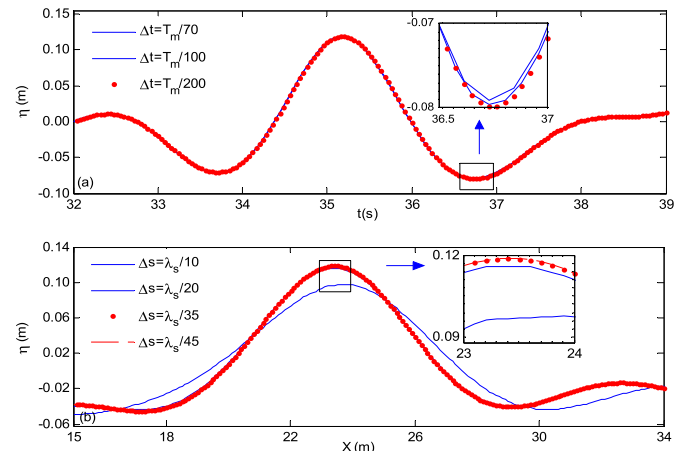


Fig. 4. Convergence tests for (a) time step and (b) mesh size.

simulations. The time step and mesh size convergent tests were also carried out for nonlinear water waves by Ma and Yan (2009) and the results converged with similar mesh size and time step.

4.2. Numerical validation

The focusing wave simulations are validated against a series of physical tests carried out in the towing tank in Harbin Engineering University. 24 wave gauges were arranged along the length of the physical tank, and the interval between two neighboring gauges was 0.4m. When the focusing position parameter x_f was specified as 30m, 40m and 50m, the far left wave gauge in Fig. 1 was correspondingly deployed at 21.905m, 31.495m and 38.905m away from the wave flap to capture the focusing wave crest. In the simulations, wave surface is recorded at 1100 points across the numerical wave tank with the interval of 0.1m.

For the case based on the QCWA spectrum (similar to the LWAL spectrum), with $A_f = 0.2\text{m}$, $x_f = 50\text{m}$, $f_n = 0.1587\text{--}0.5882\text{Hz}$, $t_f = 36\text{s}$, and $N = 32$, the validation of temporal and spatial wave surface against the measured data is presented. The comparison of the time history of wave surface at $x = 45.305\text{m}$ (the actual focusing position) demonstrated in Fig. 5 (a), shows a good agreement of the crest evolution and attenuation between the measured data and the simulation results. Particularly for their focusing wave crest elevations, the difference between them is about 3%. For validation results of other cases, the relative errors of focusing wave crest elevations are less than 5% and detailed comparisons are summarized in Xu (2016).

Fig. 5 (b) demonstrates the free surfaces at $t = 35.6\text{s}$ (the actual focusing time) recorded in the physical and the numerical wave tanks. It is observed that the spatial free surface simulated by the numerical wave tank has a good agreement with the measured data. Although the wave surface is slightly underestimated at the upstream of the crest, the focusing position captured by the numerical method is well agreed with the measurement with the difference smaller than 1%. For all other validation cases, the errors of the simulated focusing positions are less than 6% (Xu, 2016). According to the series of validations, the numerical wave tank used in this paper can be considered as an effective tool for focusing wave simulation and to investigate how the distributions of wave amplitudes influence focusing wave generation.

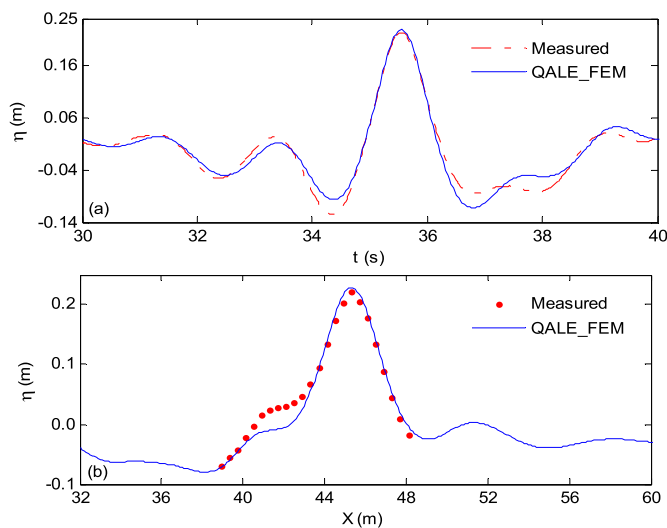


Fig. 5. Validations of the numerical wave simulation against measured data for the case of $A_f = 0.2\text{m}$, $x_f = 50\text{m}$, $f_n = 0.1587\text{--}0.5882\text{Hz}$, $t_f = 36\text{s}$, and $N = 32$ for (a) surface time history at the focusing position and (b) spatial wave free surface at focusing instant.

5. Results and discussions

In this section, the wave crest elevations and focusing positions obtained by adopting three amplitude distributions, i.e. LWAL, LWAH, CWA, under a variation of two input parameters will be discussed including (1) A_f which is the amplitude parameter for determining the amplitude of each wave component and also the target focusing wave crest elevation; and (2) f_c which is the central frequency of input wave components indicating median of the frequency range. In the following numerical tests, wave surface elevation will be recorded at 601 points along the length of numerical wave tank. The first numerical wave gauge is set at 20m away from wave maker flap, and the interval between two neighboring ones is 0.1m. The actual focusing wave crest elevation and focusing position generated in the numerical wave tank are expressed as A_f^1 and x_f^1 respectively. For all the tested cases, focusing time parameter t_f and wave component number N are specified to be 36s and 32, unless mentioned otherwise.

5.1. Free surfaces profiles of focusing waves

Based on the wave amplitude distributions as described in Section 3, focusing waves with parameters of $A_f = 0.14\text{m}$, $x_f = 50\text{m}$ and $f_n = 0.1641\text{--}0.4063\text{Hz}$ are generated in the numerical wave tank. The spatial wave free surfaces at their focusing times are compared in Fig. 6, showing different locations where the focusing wave crests occur. The results are nondimensionalized by target focusing position and crest elevation for the horizontal and the vertical axis respectively.

The focusing wave based on the LWAH distribution presents a steep crest and a deep trough, with its wave crest slightly higher (the nondimensional wave crest elevation η_{\max}/A_f being about 1.027) than those of the other two distributions. Also, moderate-sized wave crests are generated around its maximum wave crest. However, the focusing wave with the LWAL spectrum demonstrates a flat and shallow wave profile, and the wave free surface changes gently in the vicinity of the wave crest. As for the focusing wave produced by the CWA distribution, its wave crest elevation is the minimum ($\eta_{\max}/A_f = 1.015$), and the wave free surface profile up- and downstream fluctuates between the other two wave free surfaces. Above comparison suggests that the amplitude distribution of wave components not only has impact on the focusing wave crest elevation but also on the local wave free surface profile.

Crest positions of focusing waves are also altered by applying different wave amplitude distributions. The focusing wave based on the LWAH distribution occurs at the farthest position from wave maker flap, while the focusing wave of the LWAL spectrum appears at the nearest position in wave tank and the position of the CWA distribution is in between above two focusing waves.

5.2. Focusing wave crest elevations

This section will investigate the effect of wave component amplitude distribution on focusing wave crest elevations. Tests are carried out by varying two focusing wave parameters, i.e., the wave crest elevation parameter A_f and the central frequency f_c .

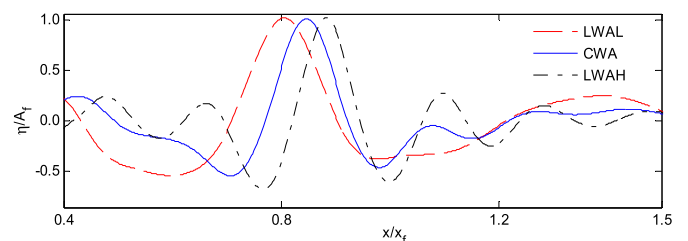


Fig. 6. Comparisons of focusing wave free surfaces for $A_f = 0.14\text{m}$, $x_f = 50\text{m}$ and $f_n = 0.1641\text{--}0.4063\text{Hz}$ under three wave amplitude distributions.

5.2.1. Focusing wave crest elevations under A_f parameters

By varying the wave crest parameter A_f from 0.05m to 0.32m, waves are generated with the frequency band of [0.1641Hz, 0.4063Hz]. The normalized crest elevations based on the amplitude distributions are plot in Fig. 7, showing that for all the amplitude distributions, the amplification of the wave crest elevation becomes more significant when the wave crest parameter increases especially for the LWAL spectrum.

When the wave crest parameter is small ($A_f < 0.15\text{m}$), three distributions result in similar wave crest elevations which are all close to the specified one with maximum 2% amplification. However, when the wave crest parameter becomes larger ($A_f > 0.15\text{m}$), the rate of the crest elevation increase becomes more significant especially for the LWAL distribution. As a result, the wave crest elevation generated by the LWAL spectrum exceeds those based on the LWAH and the CWA and reaches maximum amplification of 13% when A_f is assigned to be 0.32m. The discrepancies from elevations of other two spectra are also enlarged with increased A_f . According to the trend of focusing wave elevations in the range of small A_f values, it can be deduced that the crest elevations produced by the CWA distribution may be larger than those by the LWAL distribution for A_f being smaller than 0.05m. It is consistent with results found in Li and Liu (2015) for the comparison between focusing wave crest elevations generated by the CWA and the CWS spectrum (similar to the LWAL distribution in this research). By considering amplitude distributions over the frequency band, it can be known that, for small crest elevation parameters, different amplitude distributions have slight influence on focusing wave elevations. While for the large A_f parameters, large amplitudes being assigned to low frequency components will produce considerable amplified wave crest elevation but such phenomenon is weakened for constant amplitude distribution and large amplitudes at high frequency.

In the next section, the cause of focusing wave amplification responding to different amplitude distributions will be further analyzed. It should be noted that similar increasing crest ratio with the amplitude parameter is also presented in Baldock et al. (1996) and Ning et al. (2012) for focusing waves based on the CWA spectrum and in Xu et al. (2019) with the QCWA and the QCWS distributions. They pointed out that the increase of the crest elevations is caused by high-order wave components produced in the focusing wave generation process.

As shown in Fig. 8, the wave components of focusing waves are divided into three categories, which are the initially input wave-frequency [f_1 f_N], and extra frequencies introduced in the generation process including the lower-frequency $f_n < f_1$ and the higher-frequency $f_n > f_N$. By carrying out FFT (Fast Fourier Transform) for the generated focusing wave, the wave crest elevations corresponding to the frequency categories are also classified as A_f^L , A_f^W , and A_f^H . Within the range of the tested cases as shown in Fig. 7, here A_f values are chosen to be 0.08m,

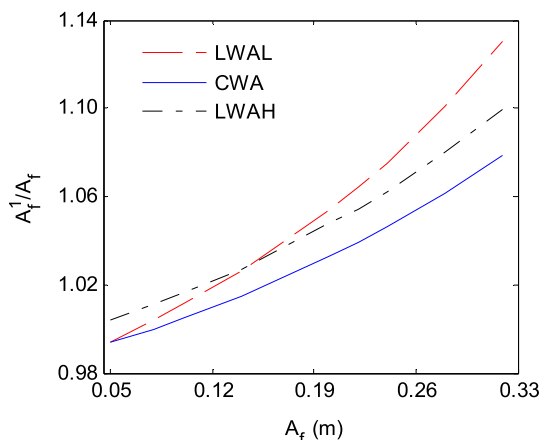


Fig. 7. Focusing wave crest elevations under A_f parameters.

0.20m and 0.32m. Wave crest elevations corresponding to wave frequency categories are demonstrated in Fig. 8.

It can be seen that, both wave-frequency and higher-frequency components produce positive wave crest elevations with the former contributes most to the focusing wave crest elevation as demonstrated in the second and fourth columns in Fig. 8. Nevertheless, lower-frequency components all produce negative wave crest elevations, which will offset part of the wave crest elevations generated by the wave-frequency and the higher-frequency components.

In the first row for small crest parameter (i.e., $A_f = 0.08\text{m}$), the crest elevations for the lower-frequency category are almost identical for different spectrum distributions, which is also the case for the wave-frequency category. While, the higher-frequency category shows a certain degree of differences, with the crest elevation of the LWAH being slightly larger than those of other two distributions. Combining the results showing in Fig. 7, for cases with small wave elevations, the effect of amplitude distribution is very limited though the focusing wave generated by the LWAH distribution has slightly higher wave crest elevation due to the higher-frequency components. For relatively large crest parameters (i.e., $A_f = 0.2\text{m}$ and 0.32m), the generated focusing wave crest elevations are dominated by the wave-frequency category, resulting in the maximum crest elevation for the LWAL distribution. The LWAH and CWA have similar results for the wave-frequency category and their crest elevations are slightly affected by the higher-frequency category. Besides, the low-frequency category shows negligible difference among the three distributions even for large A_f parameters.

The wave component amplitude and phase spectra for the generated focusing waves with $A_f = 0.2\text{m}$ are illustrated in Fig. 9. Referring to the initially input component amplitudes (the red broken line), considerable excess of the wave amplitudes is observed in Fig. 9 (a) at the higher end of the wave-frequency range, i.e. [0.35 0.40] for the CWA and LWAL distributions, which contributes to the increase of their generated focusing wave elevation. The excess of wave amplitudes may be introduced by coupling effects among wave components as found by Deng et al. (2016). For the LWAH distribution, the wave-frequency amplitudes are nearly the same with the correspondingly assigned ones but its higher-frequency components demonstrate an apparent higher focusing level as shown in Fig. 9(b), leading to maximum crest elevation in this frequency category as illustrated in the third column in Fig. 8. Thus, focusing wave crest elevations based on the LWAH being higher than initially assigned crest elevations is likely caused by the higher-frequency category.

Because the phase values of all lower-frequency wave components are negative but the amplitudes are all positive, the corresponding wave crest elevations as a production of the amplitude and the phase become negative and are consistent with the results in the first column of Fig. 8. This is similar to the 'set-down' phenomenon appearing in evolution of a wave group (Zou, 2005) and may relates to bound long waves in a focusing wave group (Sriram et al., 2015).

Moreover, the modulational instability of the above cases was also assessed based on the Benjamin-Feir Index (BFI). Their BFIs are summarized in Table A of the Appendix. According to the BFIs of the cases with corresponding A_f value, it is found that the wave amplitude distribution of focusing waves influences the BFIs, i.e., wave instability. Generally, the cases based on the LWAH distribution have the larger BFI values, compared with the ones under the other two spectra, which means the modulational stability may become serious. In Fig. 8, the focusing wave cases under the LWAH distribution have the smallest wave-frequency crest elevation A_f^W and the largest A_f^H is possibly related to modulational instability. The wave energy being at wave-frequency interval may transfer to the higher frequency sidebands. However, considering the generated focusing wave crest elevations are mainly from the wave-frequency components and the BFIs are smaller than one, it is inferred that generation results of focusing waves in this Section are dominated by dispersion focusing of wave energy, rather than the modulational instability.

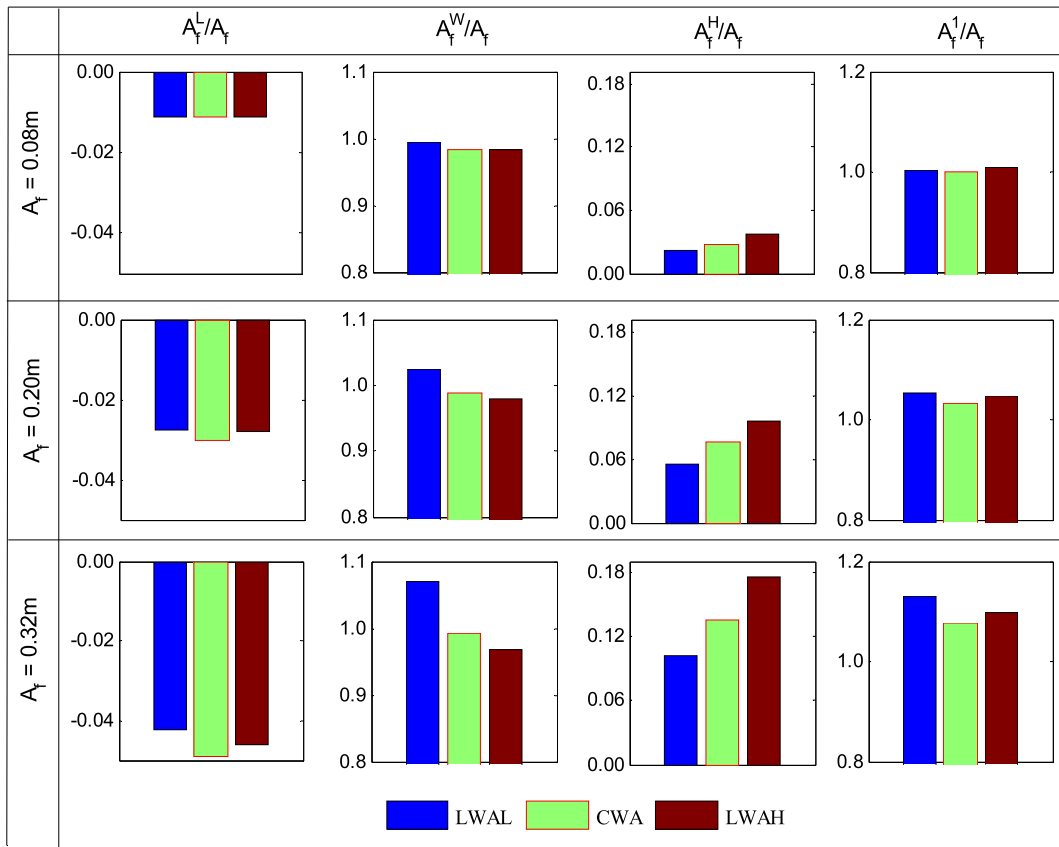


Fig. 8. Wave crest elevations corresponding to lower, initially given and higher wave frequency categories in the first, second, and third columns respectively. The overall crest elevations are in the last column. Three rows stand for crest elevation distribution for given target crest elevations of 0.08m, 0.20m and 0.32m. Three bars correspond to three amplitude distributions adopted for focusing wave generation.

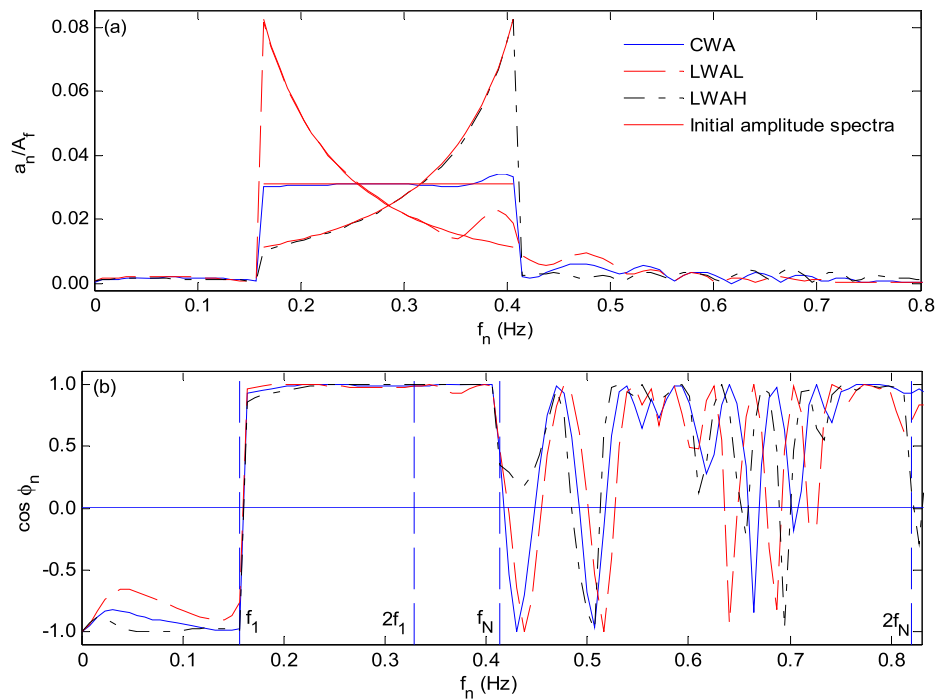


Fig. 9. Comparisons of initial assigned and the generated (a) wave component amplitude spectra and (b) wave component phase spectra for the case with $A_T = 0.2\text{m}$.

5.2.2. Focusing wave crest elevations under f_c values

In this section, focusing wave crest elevations based on amplitude distributions continue to be investigated with a series of f_c values by shifting the frequency band with the same bandwidth from low to high frequency domains. For all the cases in this section, their wave crest parameter A_f is fixed to be 0.14m. By keeping bandwidth of frequency ranges constant, i.e., $\Delta f = 0.2422\text{Hz}$, frequency ranges are shifted with their central frequencies being from 0.2461Hz to 0.3242Hz.

As shown in Fig. 10, focusing wave crest elevations overall is less sensitive to frequency ranges than to wave amplitude distributions. When comparing with the three amplitude distributions, wave crest elevations generated by the LWAL are the highest, those produced by the LWAL and the CWA are in the middle and the lowest respectively.

To further analyze focusing wave crest elevations for different f_c values, wave components corresponding to three frequency categories for the three representative cases are discussed. The definitions for the three crest elevations, A_f^I , A_f^W , and A_f^H are the same as those in Section 5.5.1.

As shown in Fig. 11, similar as results with various wave crest parameters as shown in Fig. 8, the lower-frequency components all produce negative wave crest elevations, while both their wave-frequency components and higher-frequency components contribute positive ones.

For all the amplitude distributions, the wave crest elevations generated by the wave-frequency components, i.e. the second column in Fig. 11, contribute most to their focusing wave crest elevations. For the LWAL distribution, the crest elevations from the wave-frequency are the maximum comparing to other two distributions for all central frequencies, which is also the case for the overall crest elevation even though the contribution from the higher-frequency components varies. For the LWAH and CWA distributions, their crest elevations from the wave-frequency are similar and the overall focusing crest elevations are sometimes affected by their higher-frequency components. Especially for the central frequency of 0.2852Hz, due to the large crest elevation generated by the higher-frequency components for the LWAH distribution, its focusing wave crest elevation is obviously increased, which surpasses the elevation based on the CWA distribution and gets close to the maximum elevation based on the LWAL distribution. The contribution from the higher-frequency for the LWAH also explains the increase of the crest elevation in the central frequency range from 0.28Hz to 0.30Hz in Fig. 10.

Additionally, the modulational stability of focusing wave cases investigated in this section has been evaluated in Table B of the Appendix. It closely correlates to the wave amplitude distribution adopted. For the cases with each f_c value, the focusing waves based on the LWAH distribution always have the largest BFI, whereas those of the LWAL have the smallest one. With the f_c shifting towards high frequency

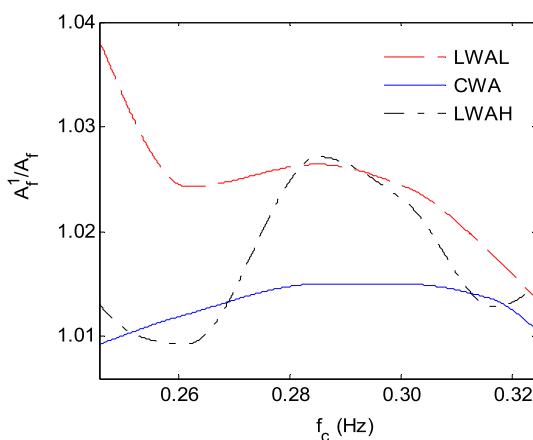


Fig. 10. Focusing wave crest elevations for f_c ranging from 0.2461Hz to 0.3242Hz.

domain, the BFIs of all the cases increasingly become large, but they are smaller than one. Moreover, from Fig. 11 it is known that the wave crest elevations from wave-frequency components occupy the most of the corresponding focusing wave crest elevations. Thus, the generation of focusing waves investigated in this section is also mainly led by the space-time focusing of wave energy.

5.3. Focusing wave positions

In this section, generation positions of focusing waves based on the three amplitude distributions are investigated for a range of wave crest parameters and central frequencies. The focusing position in this research is where the maximum crest elevation of the focusing wave occurs, which is commonly deviated from the initially specified position of x_f . In the following discussions, the positions of the actually generated focusing waves, x_f^I , will be nondimensionalized by their specified x_f values.

5.3.1. Focusing positions under A_f parameters

By running the same set of cases as in Section 5.2.1, generation positions are plotted against crest elevation parameters for three amplitude distributions in Fig. 12.

The focusing positions of the generated focusing waves are all underestimated, with x_f^I/x_f being kept smaller than one for the whole range of A_f parameter, but at different levels for different amplitude distributions. The LWAH distribution leads to the smallest deviation from the initial setting position and other two spectra lead to the focusing waves occurring more upper stream which phenomena are also pointed out by Li and Liu (2015).

The upstream shift of focusing positions is also observed in Xu et al. (2019) and Yan and Ma (2012), in their physical wave tank tests and in numerical simulations respectively. For linear wave generation by the wave maker, the progressive wave surface phase at far fluid field will be shifted $-\pi/2$ relative to that at the wave maker. For regular waves, if the expected wave crests are generated at position of x_f , the actual positions will be shifted to the downstream locations. Such phase modification of the wave free surface may also apply to the focusing wave, leading to the shift of focusing position.

However, a downstream shift of generating positions is observed by Ning et al. (2009) and Baldock et al. (1996), and they claimed it was introduced by the wave nonlinearity. Here the effect of wave amplitude distributions on focusing position will be analyzed from two aspects, phase modification of free surfaces and wave nonlinearity.

By giving $A_f = 0.08\text{m}$ and $x_f = 50\text{m}$, wave component phases (i.e., $\cos\phi_n$) at different positions of the numerical wave tank are presented for distributions of LWAL, CWA and LWAH in Fig. 13 (a), (b), and (c) respectively. It is clearly seen that for each amplitude distribution, all the wave components reach the best focusing level with $\cos\phi_n$ approaches unity across the whole frequency range. For the range covering the focusing position, the focusing varies from low level with $\cos\phi_n$ much lower than unity to the optimum with $\cos\phi_n$ close to unity at the actual focusing position, and to low level again. Such focusing level variation also confirms the upstream shift from the initially assigned position of $x_f = 50\text{m}$.

To explore whether the upshift of generation positions of focusing waves follows the linear wave shift relationship and how it is associated with wave amplitude distributions, the phase modification of $-\pi/2$ on each wave component of the focusing waves is imposed to reflect of the non-correction of the generator as shown in Eq. (14). The maximum wave crest elevations due to wave components superposition at different positions are calculated using the linear wave theory for above case under the three amplitude distributions. The results show that their focusing positions are all shift to upstream places, i.e., 40.25m, 42.1m, and 43.55m corresponding to the LWAL, the CWA, and the LWAH distributions respectively. This indicates that the superposition of initially downstream shifted regular wave components leads to the final focusing

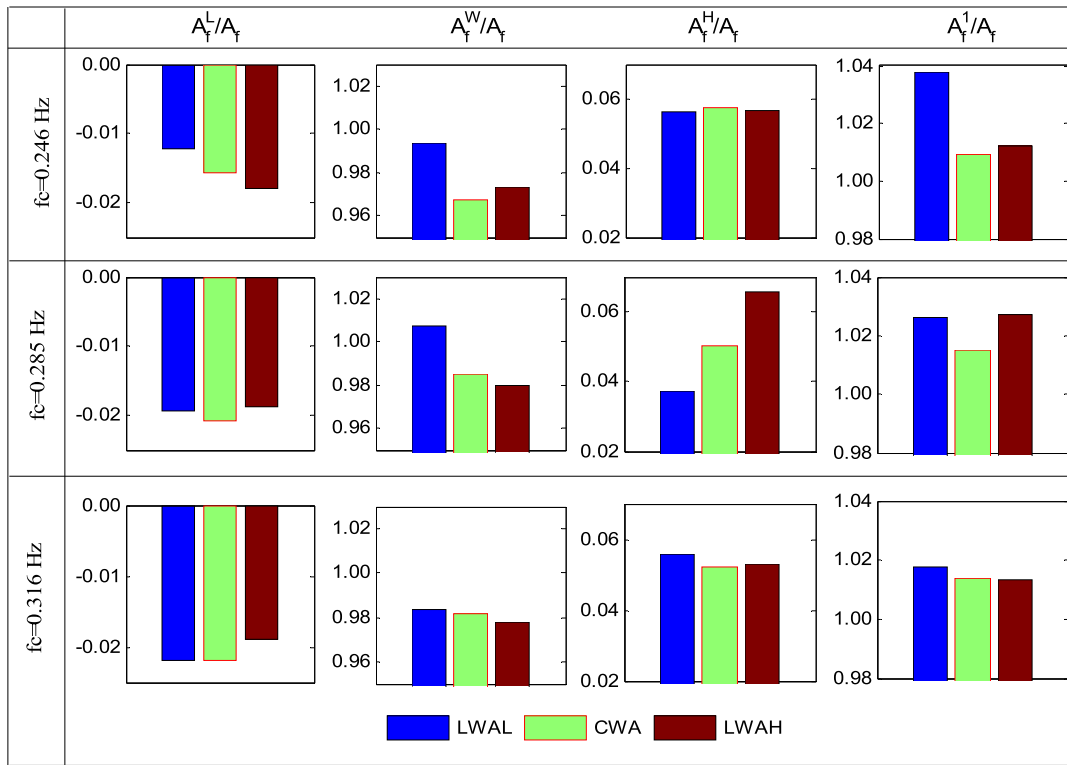


Fig. 11. Wave crest elevations generated by wave components at different frequency intervals for the cases with f_c values of 0.246Hz, 0.285Hz and 0.316Hz.

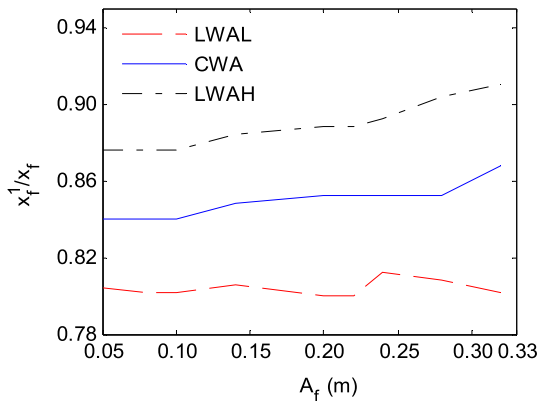


Fig. 12. Focusing positions for A_f ranging from 0.05m to 0.32m.

wave shift upstream and this shift varies for different amplitude distributions. Furthermore, considering both wave component amplitude distributions and focusing position upshifts, the larger amplitudes being assigned to low frequency components leads to the larger upshift and vice versa, it can be qualitatively deduced that the upshifts of focusing positions are correlated to the wave amplitude distribution specified. However, the quantitative estimation of contribution to the focusing position shift due to the wave surface phase needs further study.

The cases with three A_f values (i.e., 0.08m, 0.20m and 0.32m) are selected to investigate how wave nonlinearity affects generation positions of focusing waves. Local wave steepness (i.e., A_f^1/λ_x) is adopted to denote nonlinearity for the generated focusing waves. A_f^1 is the local maximum wave crest elevation measured by the wave gauge arranged at the position of x in wave tank, and λ_x is the local wave length, estimated by the local wave period around the maximum wave crest elevation in the recorded time history.

Wave steepnesses are noticeably different for three amplitude distributions as shown in Fig. 14. Wave steepness based on the LWAH

distribution is the largest for all crest elevation parameters, whereas that based on the LWAL keeps the lowest. One can deduce that local wave steepness which determines the wave local nonlinearity is significantly affected by the amplitude distribution adopted.

As shown in Fig. 14, focusing positions marked out by asterisks all occur at places where their wave steepnesses reach the maximum. Moreover, by comparing focusing positions of the three spectra, it is found the larger the local wave steepness of focusing wave is, the farther wave focuses. The LWAH spectrum leads to the maximum steepness and consequently the most downstream focusing position. Therefore, it is concluded that the focusing position is shifted downstream because of the wave nonlinearity denoted by local wave steepness which depends on wave amplitude distribution.

Besides, for each amplitude distribution wave steepness increases with the crest elevation parameter as expected, which also causes downstream shift of the focusing position. It further indicates that local wave steepness can be regarded as an indication of focusing wave nonlinearity which contributes to shift focusing positions downstream. The extent of the position shift is amplitude distribution dependent with LWAH causing the most significant shift, followed by the CWA and the LWAL in descending sequence.

For explaining wave steepness variation and consequently the variation of downstream shift caused by the amplitude distributions, wave steepnesses corresponding to wave components being at different frequency intervals are investigated. Wave components are divided into three categories according to their frequencies as Section 5.2.1, i.e., the lower-frequency components, the wave-frequency components, and the higher-frequency ones. To acquire wave steepnesses of wave components within three frequency categories, the wave surface time history recorded at focusing position is firstly decomposed into the corresponding wave components. Then the waves are regenerated based on the wave components at their frequency categories. Finally, the wave steepness for corresponding wave components (ΔS) is acquired by using local wave height and length. The wave steepnesses of the amplitude distributions are compared in Fig. 15.

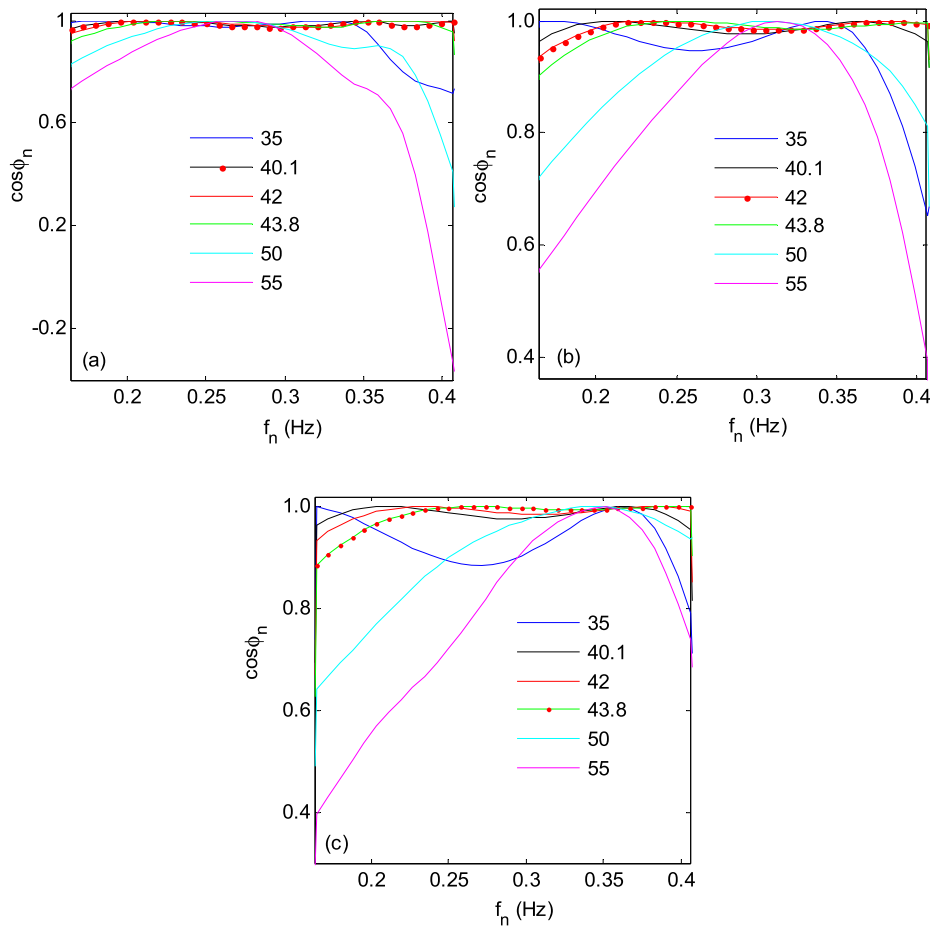


Fig. 13. Illustration of wave component phases at different positions for the case with $A_f = 0.08$ m: (a) the LWAL; (b) the CWA; (c) the LWAH ($f_n = 0.1641\text{--}0.4063\text{Hz}$; the line with dots represents for phases at corresponding focusing positions).

Fig. 15 (a) and (b) demonstrate that for all the spectra distributions, the wave steepness S (i.e., A_f^2/λ_x being at the focusing position) is mostly contributed by the components in wave-frequency category with LWAH leading to the greatest steepness and followed by the CWA and LWAL. However, for the wave-frequency category, the steepness contributions for all the spectra distributions are linearly increased with the crest elevation parameter. This is different from the trend for the overall steepness as shown in Fig. 15 (a) which shows a faster increase when crest elevation parameter increases, especially for the LWAH. The difference can be explained by the steepness from the higher-frequency components (three curves above zero steepness in Fig. 15 (c)) showing nonlinear increase of the steepness with the A_f parameter and contributing to the enlarged the gaps between the amplitude distributions. As for the components in the lower-frequency category, all wave steepnesses are negative but in very small magnitudes, having limited and similar contribution to the overall steepness.

Therefore, it is implied that focusing wave steepness values strongly depends on wave amplitude spectrum distributions. When using the amplitude spectrum with the large amplitudes being distributed at the high frequency, the focusing wave steepness is larger than that with constant distribution and also larger than that with large amplitudes allocated at the low frequency. The steepness of the focusing waves is mostly contributed by the wave components in the wave-frequency category but also affected by the components in the higher-frequency category.

5.3.2. Focusing positions under f_c values

To investigate focusing positions under f_c values, the cases selected in this section are identical as those used in the Section 5.2.2. Keeping

the frequency bandwidths constant and crest elevation parameter as $A_f = 0.14\text{m}$, their central frequencies are shifted from 0.2461Hz to 0.3242Hz . The focusing positions of these cases under the assigned amplitude distributions are compared in Fig. 16.

Overall, the focusing positions are underestimated and gradually move downstream towards the target positions with the increase of central frequency. Comparing the results from different distributions, focusing positions generated by the LWAH are the farthest from wave maker flap followed by those using CWA and LWAL for the whole range of the tested f_c . Major fluctuation can be observed for the LWAH around $f_c = 0.31\text{Hz}$, where the focusing position drops which will be explained in the following section. The deviation of the focusing position from the assigned one affected by wave amplitude distributions will be analyzed in terms of phase shift of the wave surface and wave nonlinearity associated with wave steepness.

The case with $f_c = 0.2617\text{Hz}$ has the actual focusing positions of 37.4m , 38.7m and 40m respectively for the LWAL, the CWA and the LWAH distributions. To consider the phase shift effect due to linear wave components generation and to superpose all the $-\pi/2$ shifted components, the generation positions are correspondingly 36.90m , 39.63m , and 41.67m . Consistent with the conclusion drawn in Section 5.3.1 where various crest parameters are tested, it can be deduced that the upstream shift of focusing positions can be caused by the phase shift of each linear component and their superposition, and is also dependent on the wave amplitude distribution.

The effect of wave nonlinearity on focusing positions will be analyzed using wave steepness of the cases with the central frequency ranging from 0.2617Hz to 0.3242Hz as shown in Fig. 17. It is seen that the location where the maximum local steepness occurs well matches

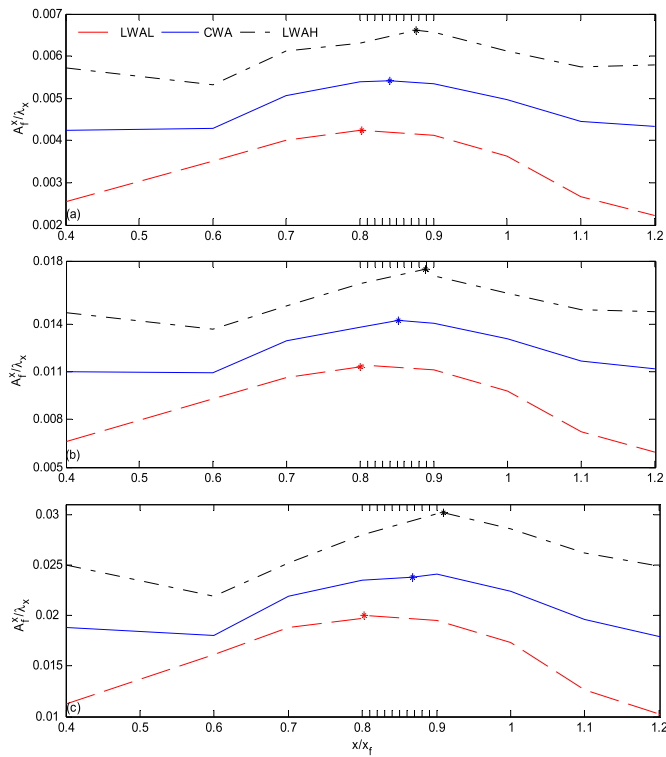


Fig. 14. Comparison of local wave steepness of the cases using amplitude distributions of LWAH, CWA and LWAL for crest parameters of (a) $A_f = 0.08\text{m}$, (b) $A_f = 0.20\text{m}$, and (c) $A_f = 0.32\text{m}$.

the focusing position as marked out by asterisks.

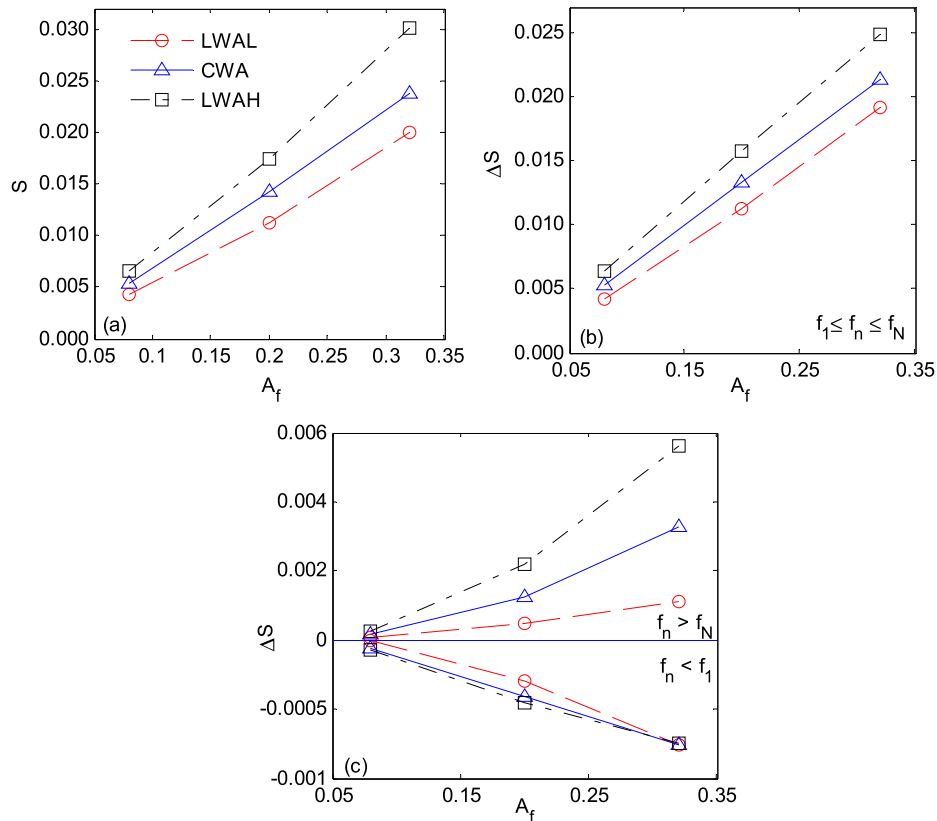


Fig. 15. Wave steepness at the focusing position for the spectra of LWAL, CWA and LWAH with (a) all wave components, (b) wave-frequency components, and (c) higher- and lower-frequency components.

Wave steepness (i.e., S being at focusing position) and its compositions (ΔS) produced by wave components as defined in Section 5.3.1 are further illustrated in Fig. 18. The trend of overall steepness is consistent with that of wave-frequency steepness, increasing with the central frequency. The comparison of wave steepness S based on three amplitude distributions is also consistent with that of corresponding wave-frequency steepnesses, the maximum for LWAH followed by those for the CWA and LWAL. For all the amplitude distributions, the overall wave steepnesses are dominated by their wave-frequency components, and receive limited positive contribution from the higher-frequency components ($f_n > f_N$) and even smaller negative contribution from the lower-frequency components.

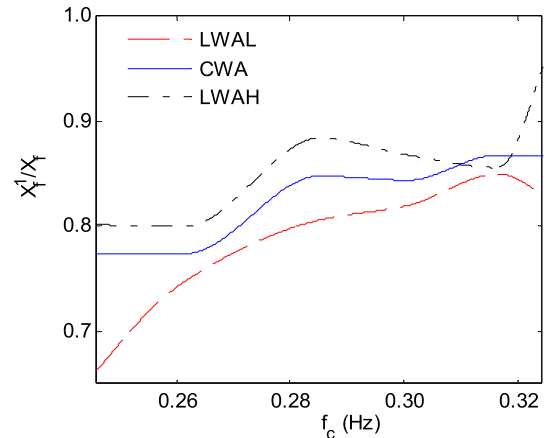


Fig. 16. Focusing positions against central frequency f_c for amplitude distributions of LWAL, CWA and LWAH.

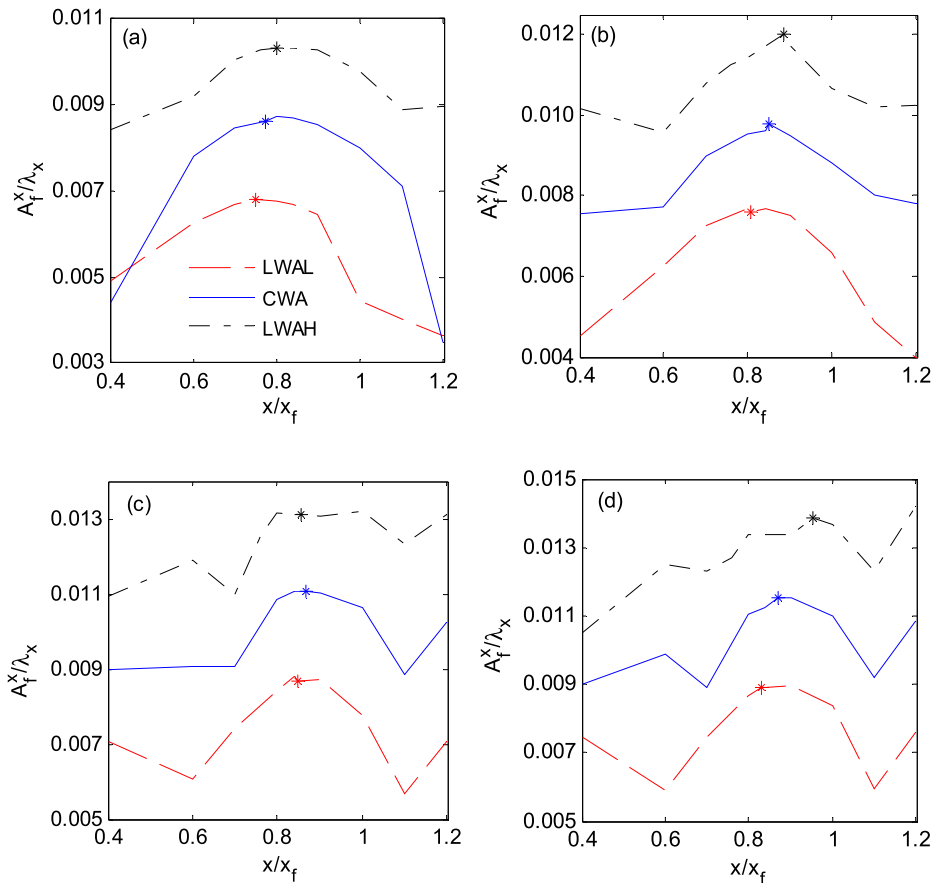


Fig. 17. Comparison of local wave steepness for various central frequencies f_c of (a) $f_c = 0.2617$ Hz, (b) $f_c = 0.2852$ Hz, (c) $f_c = 0.3164$ Hz, and (d) $f_c = 0.3242$ Hz.

Besides, a sudden drop of the higher-frequency steepness for the LWAH at $f_c = 0.3164$ Hz in Fig. 18 (c) introduces a slight falling fluctuation of its wave steepness S in Fig. 18 (a). Owing to focusing positions are positively correlated to the wave steepness, the decrease of the focusing position for LWAH around $f_c = 0.31$ Hz in Fig. 16 may be caused by the higher-frequency components.

6. Conclusions

This paper numerically investigates the effects of amplitude distribution of wave components on focusing wave generation, including the focusing wave crest elevation and the focusing position. Wave amplitude spectra with three types of variation across the frequency range (i.e., the LWAL, the CWA, and the LWAH) are constructed. Focusing waves based on the constructed amplitude distributions with the crest elevation parameter range of 0.05m–0.32m and the central frequency range of 0.2461Hz–0.3242Hz are numerically generated by the FNPT model, which is solved by the QALE-FEM. Within the given ranges of amplitude parameter (which determines the wave energy) and the central frequency for the fixed frequency bandwidth, focusing wave elevations and focusing positions are analyzed for each amplitude distribution by decomposing the focusing wave and comparing the contributions of wave components at each frequency intervals to the final wave elevation and the position. All the findings will help for amplitude spectra type selection or construction for efficiently generating tailored focusing waves (or extreme waves) in physical or numerical wave tank. The main conclusions are as follows:

- (1) With all the generated focusing wave crest elevation greater than the target, the effects of wave amplitude distributions vary with wave crest elevation parameter and frequency domain specified.

When the target wave is assigned by a small amplitude parameter or a high frequency domain, wave amplitude spectra perform similar on the generated focusing wave crest elevations. However, when the target wave is assigned by a large amplitude parameter or at a low frequency domain, wave amplitude distributions make a considerable difference on final the wave crest elevation. Generally, the LWAL distribution generates the largest wave crest elevations, whereas the CWA generates the smallest wave crests. In addition, the gap of focusing wave crest elevations based on different spectra distributions increases with the crest elevation parameter.

- (2) The focusing positions are all below the target positions with the those based on LWAH being the closest to the target and followed by those based on the CWA and LWAL. For all the amplitude spectra, the focusing position has limited change with the amplitude parameter but sees an increase with the central frequency. This is because when large amplitudes are allocated at high frequencies, such as LWAH, the contribution to the upstream shift due to phase shift becomes smaller and the contribution to the downstream shift due to the nonlinearity gets greater.
- (3) The generated focusing wave always comprises wave components beyond the initially specified frequency band, which are in lower-frequency and higher-frequency intervals. For all the amplitude distributions, the effect of lower-frequency wave components may be neglected on either focusing wave elevation or focusing position as they make small negative contributions to focusing wave crest elevations, and produce relatively limited negative wave steepness. The wave components at initially specified wave-frequency interval dominate the generated wave crest elevation and focusing position. The LWAL distribution can result in much higher wave elevation by producing larger amplitudes for the

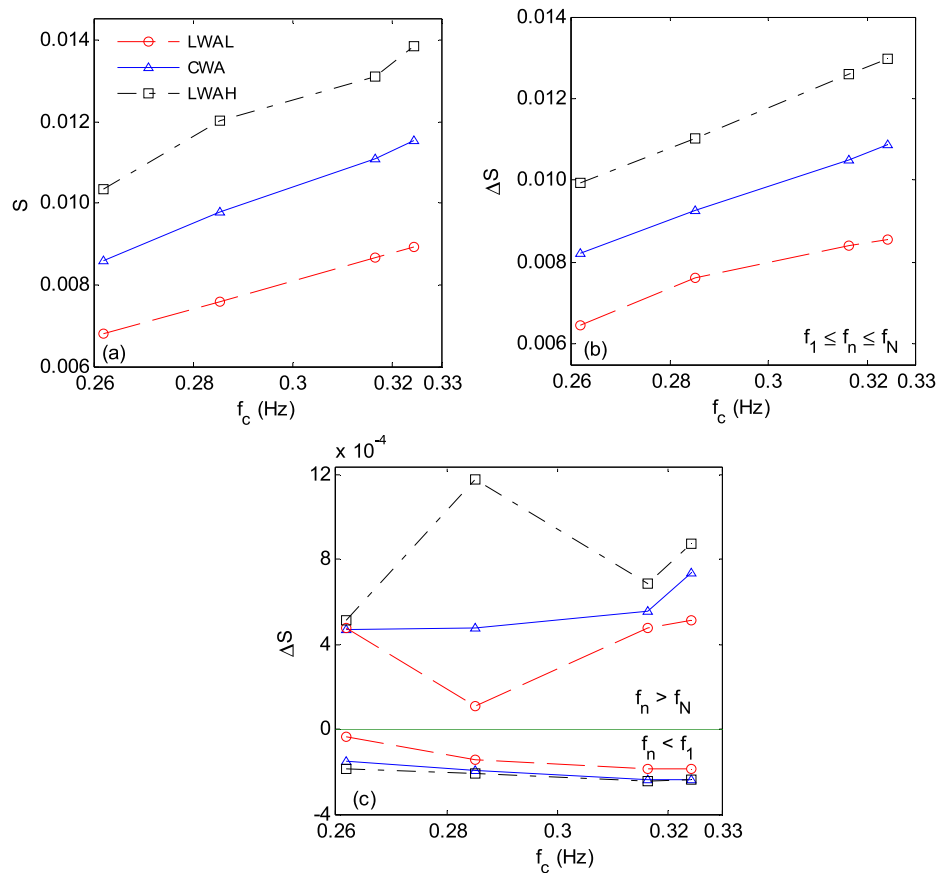


Fig. 18. Wave steepnesses of three amplitude distributions of LWAL, CWA and LWAH against f_c values for (a) the whole range of frequencies, (b) the wave-frequency interval, (c) the lower-frequency and the higher-frequency intervals.

wave component at the high end of wave-frequency interval. Due to smallest wave steepness based on the components in wave-frequency interval, i.e. the weakest nonlinearity, the LWAL also leads to the largest upstream shift of the focusing position. Moreover, the wave components in the higher-frequency interval contribute to increase crest elevation and downstream shift the focusing position, especially for the distribution has high amplitudes in high frequencies, such as LWAH.

Data curation.

Declaration of competing interest

The authors declare that they have no known competing financial interests or personal relationships that could have appeared to influence the work reported in this paper.

CRediT authorship contribution statement

Guochun Xu: Conceptualization, Methodology, Software, Writing – original draft. **Yan Zhou:** Formal analysis, Validation, Writing – review & editing. **Shiqiang Yan:** Data curation, Methodology. **Ningbo Zhang:**

Acknowledgments

This work is supported by the National Natural Science Foundation of China (Grant No. 51909125) and the Zhejiang Provincial Natural Science Foundation of China (Grant No. LY21E090002).

Appendix

The focusing wave cases involved in Section 5 of this study are summarized in Table A and Table B. The nonlinear focusing of all cases is evaluated by Benjamin-Feir Index (BFI) as Eq (a1), proposed by Serio et al. (2005).

$$BFI = \frac{\epsilon}{\Delta\omega/\omega_0} \nu \sqrt{\frac{|\beta|}{\alpha}} \tag{a1}$$

where ϵ is the characteristic wave steepness, and ω_0 is the dominant frequency, estimated by the weighted integral of the wave spectral density function. Using the linear dispersion relation, the dominant wave number k_0 could be solved. β , α and ν are functions of $k_0 \cdot d$. For brevity, their formulations are not given here. If need, they can be found in Serio et al. (2005).

Table A
the focusing wave cases used in Section 5.2.1 and 5.3.1

Group NO.	Inputting Parameters of Focusing Waves $f = 0.1641\text{--}0.4063\text{Hz}$; $k_n \cdot d = 0.657\text{--}2.366$			
	A_f (m)	Wave amplitude spectra	BFI (wave group)	BFI _{max} (all components)
1	0.05	LWAL	0	0.01259
		CWA	0	0.03435
		LWAH	0.00643	0.09056
2	0.08	LWAL	0	0.02014
		CWA	0	0.05496
		LWAH	0.01030	0.14491
3	0.10	LWAL	0	0.02518
		CWA	0	0.06870
		LWAH	0.012876	0.18113
4	0.14	LWAL	0	0.03525
		CWA	0	0.09618
		LWAH	0.01802	0.25359
5	0.20	LWAL	0	0.05037
		CWA	0	0.13740
		LWAH	0.02575	0.36227
6	0.22	LWAL	0	0.05540
		CWA	0	0.15115
		LWAH	0.02832	0.39850
7	0.24	LWAL	0	0.06044
		CWA	0	0.16489
		LWAH	0.030903	0.43473
8	0.28	LWAL	0	0.070519
		CWA	0	0.19237
		LWAH	0.03605	0.50718
9	0.32	LWAL	0	0.080593
		CWA	0	0.21985
		LWAH	0.041204	0.57964

Table B
the focusing wave cases used in Section 5.2.2 and 5.3.2

Group NO.	Inputting Parameters of Focusing Waves $A_f = 0.14\text{m}$			
	f_c (Hz)	Wave amplitude spectra	BFI (wave group)	BFI _{max} (all components)
1	0.2461 $k_n \cdot d = 0.4871\text{--}1.9743$	LWAL	0	0.02347
		CWA	0	0.06405
		LWAH	0.01185	0.16887
2	0.2617 $k_n \cdot d = 0.5536\text{--}2.1246$	LWAL	0	0.02777
		CWA	0	0.07577
		LWAH	0.01412	0.19978
3	0.2852 $k_n \cdot d = 0.6575\text{--}2.3666$	LWAL	0	0.03525
		CWA	0	0.09618
		LWAH	0.01802	0.25359
4	0.3007 $k_n \cdot d = 0.7300\text{--}2.5391$	LWAL	0	0.04108
		CWA	0.00327	0.11207
		LWAH	0.02106	0.29547
5	0.3164 $k_n \cdot d = 0.8056\text{--}2.7203$	LWAL	0	0.04765
		CWA	0.00551	0.12999
		LWAH	0.02449	0.34272
6	0.3242 $k_n \cdot d = 0.8446\text{--}2.8142$	LWAL	0	0.05122
		CWA	0.00645	0.13975
		LWAH	0.02637	0.36845

Besides BFIs of focusing wave groups, ones among their wave components are also calculated. The corresponding maximums of the cases are listed in the last column of above each table. It should be noted that BFIs are assigned to be zero if the values of $k_0 \cdot d$ are smaller than 1.36.

References

- Ai, C., Ding, W., Jin, S., 2014. A general boundary-fitted 3D non-hydrostatic model for nonlinear focusing wave groups. *Ocean Eng.* 89, 134–145.
- Baldock, T., Swan, C., Taylor, P., 1996. A laboratory study of nonlinear surface waves on water. *Philos. Trans. R. Soc. A Math. Phys. Eng. Sci.* 354, 649–676.
- Biesel, F., Suquet, F., 1951. Les appareils générateurs de houle en laboratoire. *La Houille Blanche* (5), 723–737.
- Chabchoub, A., Hoffmann, N., Onorato, M., Akhmediev, N., 2012. Super rogue waves: observation of a higher-order breather in water waves. *Phys. Rev. X* 2 (1), 011015.
- Chabchoub, A., Peri, R., Homann, N., 2014. Dynamics of unstable Stokes waves: a numerical and experimental study. In: *Proceedings of the 33rd International Conference on Ocean, Offshore and Arctic Engineering*, San Francisco, CA, USA.
- Chaplin, J.R., 1996. On frequency-focusing unidirectional waves. *Int J. Offshore Polar.* 6 (2), 7.
- Clauss, G.F., Bergmann, J., 1986. Gaussian wave packets - a new approach to seakeeping test of ocean structures. *Appl. Ocean Res.* 8 (4), 190–206.
- Clauss, G.F., Klein, M., 2011. The new year wave in a seakeeping basin: generation, propagation, kinematics and dynamics. *Ocean Eng.* 38 (14–15), 1624–1639.
- Clauss, G.F., Schmittner, C.E., Klein, M., 2006. Generation of rogue waves with predefined steepness. In: *25TH International Conference on Offshore Mechanics and Arctic Engineering*. OMAE, Hamburg, Germany. June 4, 2006 - June 9, 2006.

- Davis, M.C., Zarnick, E.E., 1964. Testing ship models in transient waves. In: 5th Symposium on Naval Hydrodynamics.
- Deng, Y., Yang, J., Zhao, W., Li, X., Xiao, L., 2016. Freak wave forces on a vertical cylinder. *Coast. Eng.* 114, 9–18.
- Didenkulova, E., 2020. Catalogue of rogue waves occurred in the world ocean from 2011 to 2018 reported by mass media sources. *Ocean Coast Manag.* 188, 105076.
- Fochesato, C., Grilli, S., Dias, F., 2007. Numerical modeling of extreme rogue waves generated by directional energy focusing. *Wave Motion* 44 (5), 395–416.
- Fujimoto, W., Waseda, T., Webb, A., 2019. Impact of the Four-Wave Quasi-Resonance On Freak Wave Shapes in the Ocean. *Ocean Dynamics* 69 (1), 101–121.
- Gong, J., Yan, S., Ma, Q., Li, Y., 2021. Numerical simulation of fixed and moving cylinders in focusing wave by a hybrid method. *Int. J. Offshore Polar* 31 (1), 102–111.
- Greenhow, M., Vinje, T., Brevig, P., Taylor, J., 1982. A theoretical and experimental study of the capsizing of salter's duck in extreme waves. *J. Fluid Mech.* 118 (MAY), 221–239.
- Hennig, J., 2005. Generation and Analysis of Harsh Wave Environments. Ph.D. Thesis. Technical University of Berlin, Berlin, Germany.
- Khait, A., Shemer, L., 2018. Application of boundary element method for determination of the wavemaker driving signal. In: ASME 2018 37th International Conference on Ocean, Offshore and Arctic Engineering.
- Kharif, C., Pelinovsky, E., 2003. Physical mechanisms of the rogue wave phenomenon. *Eur. J. Mech. B Fluid* 22 (6), 603–634.
- Kharif, C., Giovanangeli, J.P., Touboul, J., Grare, L., Pelinovsky, E., 2008. Influence of wind on extreme wave events: experimental and numerical approaches. *J. Fluid Mech.* 594, 209–247.
- Klein, M., Clauss, G.F., Rajendran, S., Guedes Soares, C., Onorato, M., 2016. Peregrine breathers as design waves for wave-structure interaction. *Ocean Eng.* 128, 199–212.
- Klein, M., Clauss, G., Hoffmann, N., 2021. Introducing envelope soliton solutions for wave-structure investigations. *Ocean Eng.* 234, 109271.
- Kuehnlein, W.L., Clauss, G.N.F., Hennig, J., 2002. Tailor made freak waves within irregular seas. In: ASME 2002 21st International Conference on Offshore Mechanics and Arctic Engineering.
- Li, J., Liu, S., 2015. Focused wave properties based on a high order spectral method with a non-periodic boundary. *China Ocean Eng.* 29 (1), 1–16.
- Ma, Q.W., Yan, S., 2006. Quasi-ALE finite element method for nonlinear water waves. *J. Comput. Phys.* 212 (1), 52–72.
- Ma, Q.W., Yan, S., 2009. QALE-FEM for numerical modelling of non-linear interaction between 3D moored floating bodies and steep waves. *Int. J. Numer. Methods Eng.* 78 (6), 713–756.
- Ma, Q.W., 2008. A New Meshless Interpolation Scheme for MLPG-R Method. *CMES-Computer Modeling in Engineering & Sciences* 23 (2), 75–89.
- Ma, Q.W., Wu, G.X., Eatock Taylor, R., 2001. Finite element simulations of fully non-linear interaction between vertical cylinders and steep waves. Part 2: numerical results and validation. *Int. J. Numer. Methods Fluid.* 36 (3), 287–308.
- Manolidis, M., Orzech, M., Simeonov, J., 2019. Rogue wave formation in adverse ocean current gradients. *J. Mar. Sci. Eng.* 7 (2).
- Ning, D.Z., Zang, J., Liu, S.X., Eatock Taylor, R., Teng, B., Taylor, P.H., 2009. Free-surface evolution and wave kinematics for nonlinear uni-directional focused wave groups. *Ocean Eng.* 36 (15–16), 1226–1243.
- Ning, D., Zhuo, X., Hou, T., Teng, B., 2012. Numerical investigation of focused waves on uniform currents. In: 22nd International Offshore and Polar Engineering Conference. ISOPE-2012, Rhodes, Greece. June 17, 2012 - June 22, 2012.
- Niu, X., Ma, X., Ma, Y., Dong, G., 2020. Controlled extreme wave generation using an improved focusing method. *Appl. Ocean Res.* 95, 102017.
- Onorato, M., Suret, P., 2016. Twenty years of progresses in oceanic rogue waves: the role played by weakly nonlinear models. *Nat. Hazards* 84, S541–S548.
- Ma, Q.W., Yan, S.Q., Greaves, D., Mai, T., Raby, A., 2015a. Numerical and experimental studies of Interaction between FPSO and focusing waves. In: The Twenty-Fifth International Ocean and Polar Engineering Conference. Kona, Hawaii, USA.
- Schmittner, C., Kosleck, S., Hennig, J., 2009. A phase-amplitude iteration scheme for the optimization of deterministic wave sequences. In: ASME 2009 28th International Conference on Ocean, Offshore and Arctic Engineering.
- Serio, M., Onorato, M., Osborne, A.R., Janssen, P.A., 2005. On the computation of the benjamin-feir Index. *Il Nuovo Cimento C* 28 (6), 893–903.
- Shemer, L., 2015. Advantages and limitations of the nonlinear schrödinger equation in describing the evolution of nonlinear water-wave groups. *Proc. Est. Acad. Sci.* 64 (3S), 356–360.
- Shemer, L., Ee, B.K., 2015. Steep Unidirectional Wave Groups - Fully Nonlinear Simulations Vs Experiments. *Nonlinear Processes in Geophysics* 22 (6), 737–747.
- Shemer, L., Jiao, H., Kit, E., Agnon, Y., 2001. Evolution of a nonlinear wave field along a tank: experiments and numerical simulations based on the spatial Zakharov equation. *J. Fluid Mech.* 427, 107–129.
- Sriram, V., Schlurmann, T., Schimmels, S., 2015. Focused wave evolution using linear and second order wavemaker theory. *Appl. Ocean Res.* 53, 279–296.
- Stagonas, D., Buldakov, E., Simons, R., 2018. Experimental Generation of Focusing Wave Groups on Following and Adverse-Sheared Currents in a Wave-Current Flume. *Journal of Hydraulic Engineering* 144 (5).
- Takezawa, S., Hirayama, T., 1976. Advanced experimental techniques for testing ship models in transient water waves. Part II: the controlled transient water waves for using in ship motion tests. In: Proceedings of the 11th Symposium on Naval Hydrodynamics: Unsteady Hydrodynamics of Marine Vehicles, pp. 37–54.
- Touboul, J., Giovanangeli, J., Kharif, C., Pelinovsky, E., 2006. Freak waves under the action of wind: experiments and simulations. *Eur. J. Mech. B Fluid* 25, 662–676.
- Wu, C.H., Yao, A., 2004. Laboratory measurements of limiting freak waves on currents [J]. *Journal of Geophysical Research Oceans* 109 (C12).
- Xu, G., 2016. Research on Generation of FreakWave and its Effect on Truss SPAR Motions. Ph.D. Thesis. Harbin Engineering University, Harbin, China.
- Xu, G., Yan, S., Ma, Q.W., 2015. Modified SFDI for Fully Nonlinear Wave Simulation. *CMES-Computer Modeling in Engineering & Sciences* 106 (1), 1–35.
- Xu, G., Hao, H., Ma, Q., Gui, Q., 2019. An experimental study of focusing wave generation with improved wave amplitude spectra. *Water* 11 (12), 2521.
- Yan, S., Ma, Q.W., 2010. QALE-FEM for modelling 3D overturning waves. *Int. J. Numer. Methods Fluid.* 63 (6), 743–768.
- Yan, S., Ma, Q., 2012. Numerical study on significance of wind action on 2-D freak waves with different parameters. *J. Mar Sci Tech-Japan.* 20 (1), 9–17.
- Yuen, H.C., Lake, B.M., 1980. Instabilities of waves on deep water. *Annu. Rev. Fluid Mech.* 12 (1), 303–334.
- Zhang, H.D., Shi, H.D., Soares, C.G., 2019. Evolutionary Properties of Mechanically Generated Deepwater Extreme Waves Induced by Nonlinear Wave Focusing. *Ocean Eng.* 186, 106077.
- Zheng, Y., Lin, Z., Li, Y., Adcock, T., Li, Y., van den Bremer, T.S., 2020. Fully nonlinear simulations of unidirectional extreme waves provoked by strong depth transitions: the effect of slope. *Phys. Rev. Fluids.* 5 (6), 064804.
- Zou, Zhili, 2005. Water Wave Theories and Their Applications. CHINA SCIENCE PUBLISHING & MEDIA LTD, pp. 152–153 (in Chinese).